https://doi.org/10.5194/egusphere-2025-5764
Preprint. Discussion started: 7 January 2026

Bridging the gap between weather forecasting and tsunami forecasting: a background model of the open ocean in the tsunami spectrum

Sean R. Santellanes[1,2,*] and Diego Melgar[1]

[1]University of Oregon, Department of Earth Science, Eugene, Oregon, United States of America
[2]University of Otago, Department of Geology, Dunedin, Otago, Aotearoa New Zealand
[*]Correspondance to: Sean R. Santellanes, sean.santellanes@otago.ac.nz

Abstract. A reference power law of ω^{-2}, where ω is angular frequency, has been traditionally used to characterize the background open ocean tsunami spectrum (BOOTS) slope from a period of 10 mins to 120 mins and that its noise profile can be assumed to be normally distributed. However, this characterization is based on data from temporary deployments of bottom pressure sensors that lasted from several weeks to 11 months and only in scattered areas of the Pacific. Here we measure the BOOTS noise profile using 1-15 years of bottom pressure recorder data sampled at 15 s from the Deep-ocean Assessment and Reporting of Tsunamis (DART) stations. We utilize probabilistic power spectral density plots to create background noise models for 34 DART stations across the Pacific basin. We find that often a simple normal probability distribution does not correctly characterize the observed background noise spectrum at periods of 120 s, 250 s, 800 s, and 2700 s. We find deviations from the expected behavoir follow a strong seasonality signal due to infragravity waves. We calculate infragravity wave heights and their mean values for December, January, and February and June, July, and August. We found that meteorologically induced infragravity wave events are the largest factors in seasonal variations of the BOOTS slope and intercept, especially in the east Pacific. We show the typical meteorological systems that drive these events, and we connected tropical systems from off the coast of Mexico to infragravity wave events in the east and central Pacific. And that these infragravity wave generating events potentially affect the probability distributions of the BOOTS. Finally, we convert plot the spatial distributions of the probability distribution functions.

1 Introduction

The advent of the Deep-ocean Assessment and Reporting of Tsunamis (DART) station network ushered in the era of Pacific Basin wide observations of water level height in the open ocean (Titov et al., 2005). Nowadays, tsunami service providers (TSPs) include DART station data into their operational workflow. The inclusion of water level data has improved the diagnosing of tsunami sources, which are then used to initiate tsunami forecasts (Gica, 2008). These data have also been used in machine

https://doi.org/10.5194/egusphere-2025-5764
Preprint. Discussion started: 7 January 2026

learning (ML) and data assimilation (DA) to refine forecasts of tsunami impacts (e.g., inundation or flow velocity) (Gusman et al., 2016; Yang et al., 2019; Someya and Furumura, 2025). Improvements in understanding the uncertainties inherit to the data may help focus efforts into positively assimilating or ingesting these data for DA or ML workflows.

In the realm of DA, optimal interpolation (OI) has been shown to be effective in constraining the uncertainties in tsunami impact forecasts (Gusman et al., 2016; Yang et al., 2019). It is the DA algorithm of choice for tsunami forecasting, owing to its relatively low computational cost and computational efficiency compared to other DA algorithms (i.e., 3DVAR, 4DVAR, etc.). However, as noted by Yang et al. (2019), it performs worse than more advanced DA methods (e.g., the ensemble Kalman filter or 4DVAR). Recent advancements in computational efficiency and computational affordability have opened the door to the use of more advanced DA algorithms, but therein lies the issue. More advanced DA algorithms require knowing the observational and background errors of the measuring instruments and physical systems (Chan et al., 2020). This issue is not only limited to DA applications but also to ML applications (Mulia et al., 2022).

Applications of ML to tsunami impact forecasting usually rely on convolutional neural networks (CNNs) or recurrent neural networks (RNNs), with some works investigating the potential applications of physics informed neural networks (PINNs)(Liu et al., 2021; Mulia et al., 2022; Someya and Furumura, 2025). Within this scope, we focus our discussion on the use of synthetic events to generate tsunami waveforms for training data. CNNs and RNNs, in simplest terms, function as an inferred weighted moving average regression model. PINNs, likewise, can best be thought of as regression models whose weights are defined by a user defined norm to the physical equations of interest thereby approximating a numerical solver (Raissi et al., 2017). Therefore, synthetic waveforms, which can appear smooth due to modelling choices, will not contain valuable information necessary to accurately or precisely train the ML schemes against real world data. When noise is combined with synthetic waveforms, CNNs and RNNs see improved performances; however, this remains an open research question for PINNs. But what exactly must the character of this noise be? It is usually assumed to follow a normal (i.e., Gaussian) distribution, but how well does this approximation perform (Maeda et al., 2015)?

Rabinovich (1997) noted that the background open ocean tsunami spectrum (BOOTS) (herein we define to be the periods of 2 mins - 120 mins) spectral noise follows a reference power law of ω^{-2}, where ω is angular frequency, for the periods of 10 mins - 120 mins (or 30 min - 120 min as seen in Rabinovich (2020)). Noise from the periods of 2 min - 10 min is considered inconsequential, as the energy in this band is much less than longer periods or short period waves < 1 min. Although, it does sometimes happen where maximum tsunami height occurs when periods are less than equal to 10 mins, as can be the case for harbors and inlets. If we assume that the BOOTS slope is ω^{-2}, it can be reasonably assumed as a first guess that the noise follow a Gaussian (e.g., normal) distribution for the periods greater than 10 mins for a sufficiently long dataset by invoking the central limit theorem. The distribution for periods from 2 mins - 10 mins can likewise be said assumed to be Gaussian following the same logic, but there are many phenomena that can influence this section of the BOOTS.

There is of course a question that must be addressed: why do we care about uncertainties in the open ocean when the largest contributors of uncertainty are the tsunami source area and the nonlinear processes in shallow water? The response is quite simple! We give a simple thought experiment to elucidate the matter. Say a potentially tsunamigenic earthquake has occurred (e.g., an earthquake $\geq$M7.0, but this is a rather arbitrary condition), and that the tsunami has no confirmation until observed by

https://doi.org/10.5194/egusphere-2025-5764
Preprint. Discussion started: 7 January 2026

a DART station. The tsunami signal is obtained by de-tiding the data, with care to ensure that seismic wave contamination and other effects are minimized to obtain the crucial first arrival information. Now, the first arrival is utilized by TSPs to initiate a tsunami forecast by inverting for a tsunami source (e.g., the National Oceanographic and Atmospheric Administration's (NOAA's) short-term inundation forecasting for tsunamis (SIFT)). There will be noise in the data that is not at all related to the tsunami. As we will detail in the next paragraph, many different forcings inhabit this range of periods, but they are assumed to be constant because the energy is much less than neighboring spectral bands. But is this treatment justifiable? Roger (2024, and references therein) show that the period band of 120 s - 800 s can be influenced by atmospheric forcings, which can cause ambiguity in tsunami impact forecasting and predictability. In the fields of meteorology and atmospheric science, anything that can influence variables of interest must have their uncertainties measured to further constrain the forecast and initial conditions (Zhang et al., 2004).

A myriad of forcings (Webb et al., 1991; Aucan and Ardhuin, 2013; Rawat et al., 2014; Roger, 2024) can potentially impact the long and short periods of the BOOTS and potentially introduce deviations from the simple logic model introduced in paragraph five(Kulikov et al., 1983; Filloux et al., 1991; Webb et al., 1991; Rabinovich, 1997; Rabinovich et al., 2013). Among these, our study focuses on the effects of two: infragravity waves (IGWs) and atmospheric pressure disturbances (i.e., tropical and extra-tropical cyclones). It has been observed in previous studies that tsunami spectral can interact with these phenomena. Although, as Roger (2024) notes, these impacts have been lightly studied by the tsunami science field. We hypothesize that these impacts may impact the short periods of the BOOTS and its noise profile.

In order to characterize and test the noise of the BOOTS and the DART stations, we compile probabilistic power spectral densities (PPSDs) for each DART station over a length of time as seen in Figure 1. We analyze the distribution of power at periods of 120, 250 s, 800 s, and 2700 s; and, we calculate standard deviations, skewness, and kurtosis for each period bin. We then measure the temporal variations in the BOOTS slope between 12 mins - 120 mins. These measurements provide information about how the noise distribution affects the BOOTS slope over the meteorological seasons. We find that changes in BOOTS slope are coincident with IGW production. So, we measure IGW heights at the DART stations and show how meteorological systems can cause noise distributions to be different across the Pacific basin. Finally, we discuss how these factors can influence DA and ML applications.

2 Data and Methods

2.1 The DART station system and PPSD measurements of the BOOTS noise

To ascertain the distribution of BOOTS noise, we utilize the DART BPR quality-controlled data provided by the National Centers for Environmental Information (NCEI) (NCEI, 2005). In real-time operations, DART stations operate using event detection to trigger changes in sampling rate. This variability in sample rates is unsuitable for this study; however, the BPR component of the DART system continuously logs 15 s sampled data. This data is periodically retrieved by NOAA oceanographic vessels and archived. We thus limit our analysis to include the time periods where BPR data with a 15 s sampling rate are available (Figure 1). We do not use days where data are at sampling rates $>$ 15 s, or the data are missing. We

https://doi.org/10.5194/egusphere-2025-5764
Preprint. Discussion started: 7 January 2026

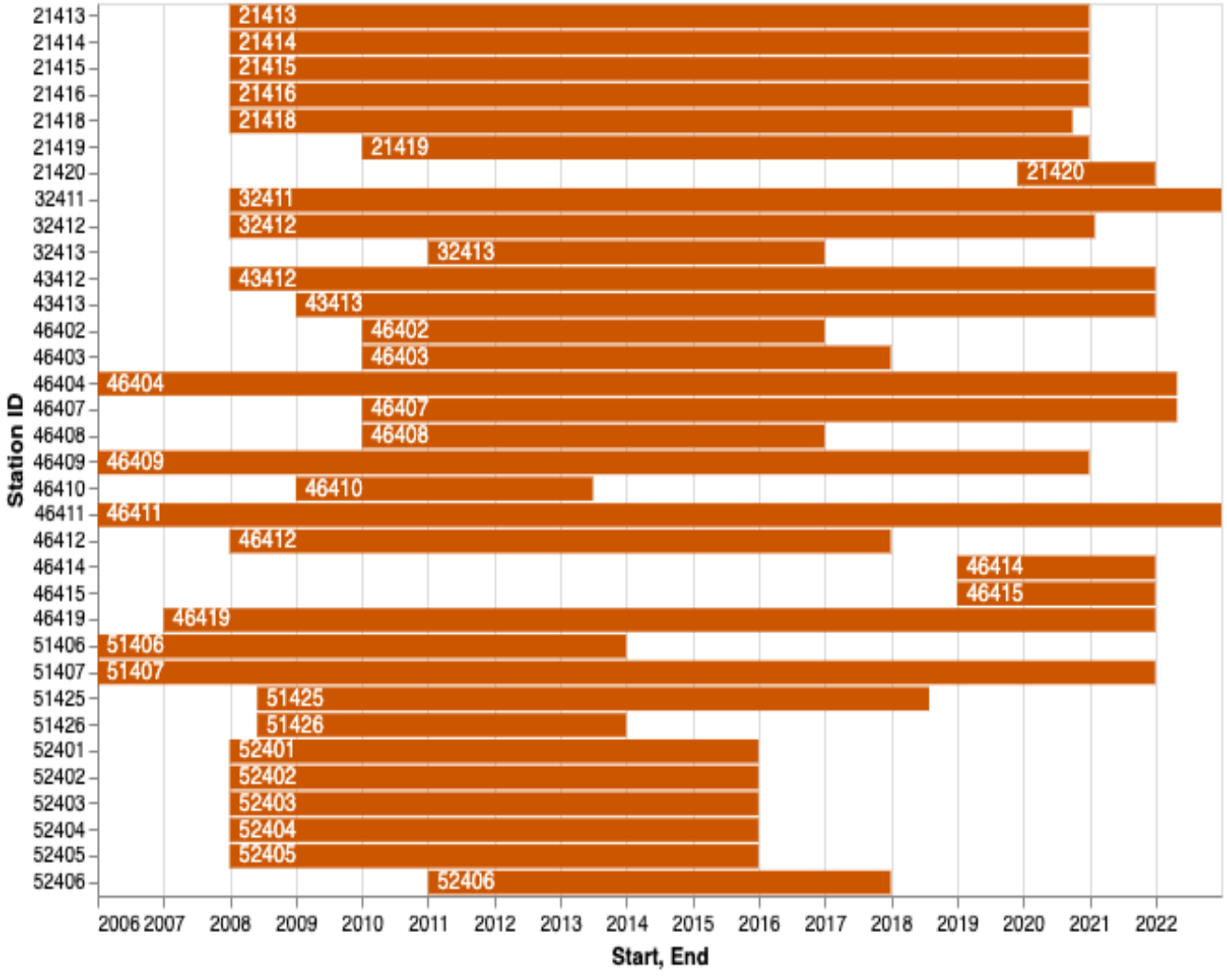

Figure 1. Station up-time graphs that show the time spans of data used for each DART in this study.

https://doi.org/10.5194/egusphere-2025-5764
Preprint. Discussion started: 7 January 2026

then ingest day long segments of the time series into the PPSD calculation following the approach detailed by McNamara and Buland (2004). This approach is desirable because it does not require any cleaning or removal of artifacts in the data. No filter or removal of tidal signals is applied to the data as they are quality-controlled the NCEI. As part of the quality-control process, the data are de-tided using a tidal and harmonic analysis (NCEI, 2005). The PPSDs are calculated for the periods of 30 s to 2 hrs for each of the 34 DART stations shown in Figure 2.

We test which probability distribution function best fits the data at the period bins of 120 s, 250 s, 800 s, and 2700 s. We limit our allowable probability distribution functions (PDFs) to normal, lognormal, skewnormal, beta, gamma, exponential, uniform, cauchy, and levy. The periods of 120 s and 250 s are selected because they are firmly in the part of the BOOTS associated with tsunami waves generated by submarine landslides, volcanic eruptions, or small earthquakes, but also, where interactions with IGWs from various generating mechanisms are frequent (Roger, 2024). The periods of 800 s and 2700 s are selected because they are outside this range, and it is where tsunami waves associated with large earthquakes tend to manifest (Roger, 2024). In order to reduce the effects of tsunamis imposed on the PDFs, we limit empirical PDF fits to data within 3 standard deviations of the mean. We do not filter out the tsunamis as detailed in the NCEI because the records are so long that they do not impact in any meaningful way the PPSD behavior!

2.2 Measuring temporal variations of the BOOTS noise

We calculate the spectral slope and intercept of the BOOTS in two week intervals with the multitaper spectral power spectral density (MT-PSD) methods detailed in Prieto (2022). We calculate the BOOTS intercept, as it provides a simple single parameter reference for the amount and type of noise present in the sampled time period (Rabinovich, 1997). We choose two week intervals to capture the apparent seasonal variations of the BOOTS. We perform a least squares fit of the BOOTS spectral slope between the periods of 12 min - 100 min, in order to minimize effects from IGW and tidal interactions (Roger, 2024). We find that, generally speaking, the PPSDs for the DART stations fit on a spectrum between two archetypal behaviors: mostly linear behavior (Figure 3a) with slope values near what the earlier literature (Kulikov et al., 1983; Filloux et al., 1991; Rabinovich, 1997) described (a shape we refer to as "convex") and those that experience a large amount of variation and departure from the log-linear model (what we refer to as "dromedary") (Figure 3b), particularly between the periods of 120 s - 800 s. The lower bound of 12 min was selected as it is the period when the dromedary shape of the PPSD (see Figure 3b) begins to taper off, and it is outside of the upper limit of 600 s (10 min) in the IGW band described by Aucan and Ardhuin (2013). We select an upper limit of 100 min to minimize any long period noise effects. As with the PPSD method, we use only data when sampling rates are at 15 s. In order to minimize tsunami effects, we do not calculate the BOOTS slope when a tsunami occurs within a two week measuring period and for the next two week period afterwards. Tsunami coda effects can be discernible for days after tsunamigenesis due to bathymetric and coastline effects both regionally (Melgar and Ruiz-Angulo, 2018) and globally(Kohler et al., 2020). We use the tsunami database provided by the NCEI to filter out tsunamis generated by earthquakes $\geq M_w$7.0, landslides, and volcanoes. This procedure ensures that we are measuring background noise.

https://doi.org/10.5194/egusphere-2025-5764
Preprint. Discussion started: 7 January 2026

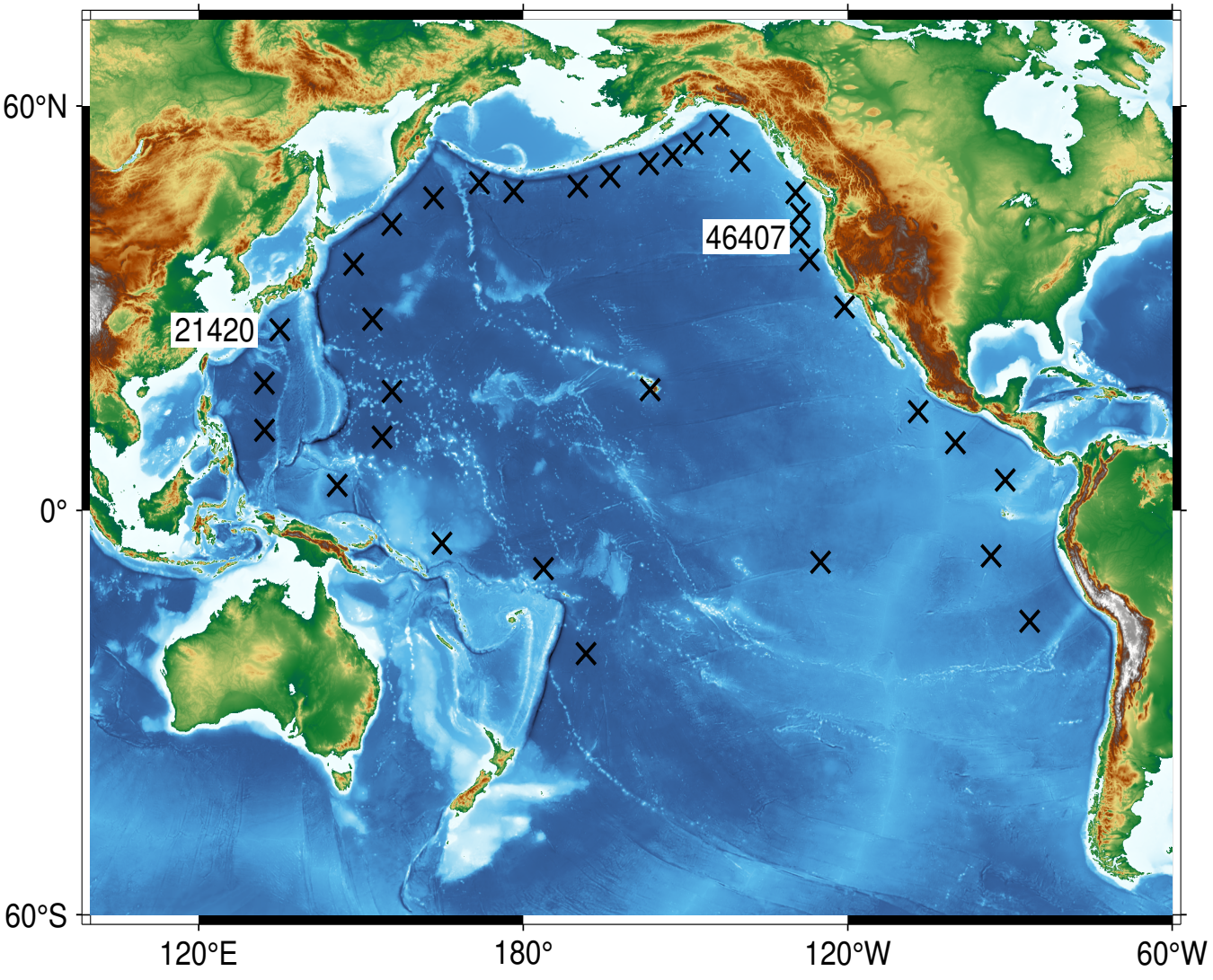

Figure 2. Crosses mark the locations of the DART stations used in this study. DARTs 21420 and 46407 are highlighted because they are emblematic (21420) and non-emblematic (46407) to the reference power law of ω^{-2} BOOTS slope values.

https://doi.org/10.5194/egusphere-2025-5764
Preprint. Discussion started: 7 January 2026

2.3 Measurement of IGWs with DART stations

Rawat et al. (2014) utilize numerical models and in situ measurements of DART data to track IGW events across the Pacific basin. There they show via tracking of IGW burst events that IGW production is highest in the area of the Cascadia Subduction Zone (CSZ), producing some of the largest IGW values in the Pacific basin. We use the data preparation method from Aucan and Ardhuin (2013) which assumes that bottom pressure recordings at IGW periods are free of pressure effects from wind-driven waves and thus that the DART BPR data can be used to extract IGW heights at those periods. Following their approach, we consider that we are examining free monochromatic waves of wavenumber k and that we can relate the bottom pressure amplitude p_b to the surface amplitude elevation a via a transfer function M, which is a function of water depth D, with the equation:

$$p_b = aM = a\frac{\rho g}{cosh(kD)}, \tag{1}$$

where ρ is water density and g is gravity acceleration. We relate wavenumber k to wave frequency f via Laplace's dispersion relation, $(2\pi f)^2 = gktanh(kD)$. We use Prieto (2022)'s multitaper code to produce power spectral densities $F_p(f)$ of the DART BPR data. The BPR data are subject to the same constraints as to when the BOOTS slope and intercept were calculated in section 2.2. The transfer function M is applied to the power spectral densities to obtain the surface elevation spectral density:

$$E(f) = M^2 F_p(f). \tag{2}$$

We then solve for the significant IGW height, which is defined as the partially integrated spectrum:

$$H_{IG} = 4\sqrt{\int_{f_{min}}^{f_{max}} E(f)df}. \tag{3}$$

We choose the same f_{min} and f_{max} as Aucan and Ardhuin (2013), setting them to 8.3×10^{-4} Hz and 1.1×10^{-2} Hz, respectively. As we did not remove tsunami signals prior to calculating the significant IGW heights, we follow the same method used for removing tsunami signals from the calculations of the BOOTS slope and intercept. For each station, we calculate the time averaged H_{IG} for the time periods of JJA and DJF.

3 Results

3.1 PPSD behavior of the BOOTS

The BOOTS intersects with what is traditionally considered the IGW band in the periods from 60 s to 600 s(Webb et al., 1991; Aucan and Ardhuin, 2013; Rawat et al., 2014; Roger, 2024). Figure 3a shows the PPSD for DART 21420 — located 480 km southeast of Miyazaki-shi, Japan, Figure 2. This station's PPSD is best emblematic of the expected behavior from the ω^{-2}

https://doi.org/10.5194/egusphere-2025-5764
Preprint. Discussion started: 7 January 2026

reference power law. Its mean slope value is 2.03 ± 0.19, and its mean intercept value is $10^{-4.48\pm0.35}$ (Table S1). We observe from Figure 3a that even for this relatively "well behaved" site the PPSD is not an exact straight line; it can have non-negligible variation of as much as 5-10 dB in the 120 s - 250 s band, giving the PPSD a convex appearance. When we examine the PDFs of these period bands, the convex shape is best explained by a beta distribution with p-values of 0.85 to 1.00. The period bins of 800 s and 2700 s do not have normally distributed data. Instead, they have PDFs best fit by the gamma and log normal distributions with p-values of 0.87 and 0.72, respectively. Even though DART 21420 follows a reference power law of ω^{-2}, the noise profile is not normally distributed.

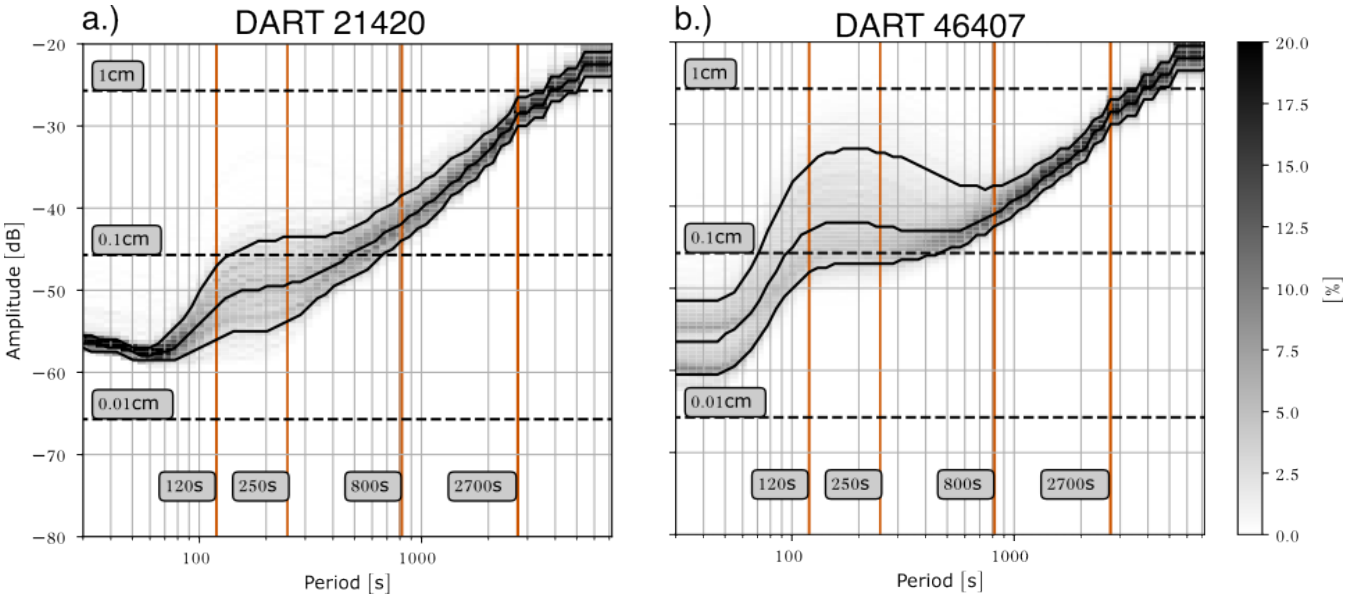

Figure 3. a.) Probabilistic Power Spectral Density (PPSD) plot for DART 21420 — emblematic of behavior that follows the reference power law of ω^{-2}. Amplitudes corresponding to noise levels of 1 cm, 0.1 cm, and 0.01 cm are shown as dashed, black lines. Periods corresponding to 120 s, 240 s, 800 s, and 2700 s are delineated by solid, burnt orange lines. b.) PPSD for DART 46407 — emblematic of behavior that does not follow the reference power law of ω^{-2}. Amplitudes corresponding to noise levels of 1 cm, 0.1 cm, and 0.01 cm are shown as dashed, black lines. Periods corresponding to 120 s, 250 s, 800 s, 2700 s are delineated by solid, burnt orange lines.

Figure 3b shows the PPSD for DART 46407 — located 390 km to the west of Coos Bay, OR (Figure 2). Its behavior is dromedary in appearance, with regard to the PPSD — a significant departure from the ω^{-2} reference power law abiding behavior demonstrated by DART 21420. Its mean slope value is 1.90 ± 0.22, and its mean intercept value is $10^{-4.25\pm0.40}$ (Table S1). Critically, Figure 3b indicates that amplitude spread for periods between 120 s - 800 s is considerable between the 10^{th} percentile and the 90^{th} percentile. The PDF fits for these period bins of 120 s and 250 s are best described by the skewnormal distribution function, with p-values of 0.000005 and 0.05. Though these p-values are low, there are the highest of the allowed potential PDF fits. Whereas, the 800 s period bin is best described by the lognormal distribution with a p-value of 0.01. The 2700 s period bin is best fit by a normal distribution with a p-value of 0.77. In contrast with DART 21420, the

https://doi.org/10.5194/egusphere-2025-5764
Preprint. Discussion started: 7 January 2026

long periods do follow a normal distribution. Lastly, DART 46407 has an enigmatic bifurcation in its PPSD for periods < 80 s. Something that is not observed in the PPSD of DART 21420 (Figure 3). Further discussion of the PDF fitting results are reserved for section 3.4.

3.2 Temporal variations in the BOOTS noise

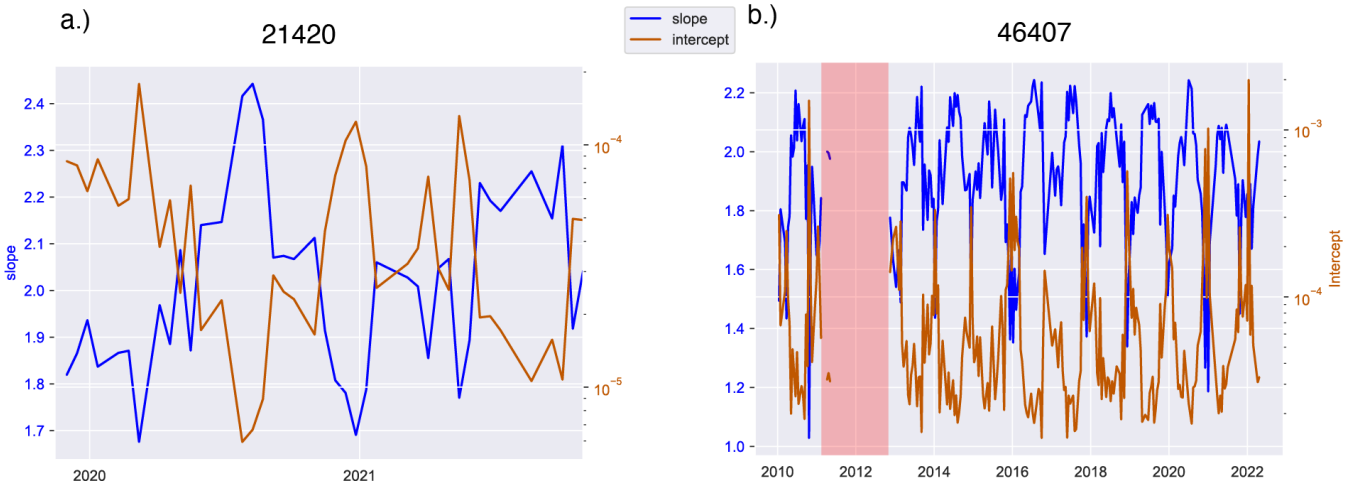

Figure 4. a.) 21420 time-series of BOOTS slope (blue) and intercept (orange). b.) 46407 time-series of BOOTS slope (blue) and intercept (orange). Period of low-quality data, resulting in no values for either parameter, is shown in red.

We observe from Figure 4a that DART 21420 experiences some amount of seasonal variation over the course of its deployment from December 2019 to October 2021. It achieves maximum slope values > 2.3 during the time period of JJA; meanwhile, it obtains minimum slope values < 1.8 during the time period of DJF. We note that there is a seemingly inverse relationship between the maximum/minimum values for the BOOTS slope and intercept. Lower magnitude intercept values have been attributed to periods of less atmospheric noise (Rabinovich, 1997), meaning periods of calm weather correspond to high BOOTS slope values. We note that the period of minimum BOOTS slope values corresponds to extratropical cyclone season for the north Pacific. However, the length of record for DART 21420 is a modest 2 years long compared to other stations we analyze (Figure 1).

Figure 4b shows a much longer 12 year time series showcasing rich seasonal variation of bottom pressure for DART 46407. It obtains maximum slope values in JJA > 2.2 and minimum slope values in DJF <1.4. While partially evident in Figure 4a, Figure 4b demonstrates more strongly the seemingly inverse nature of the BOOTS slope and intercept over a much longer period of record — January 2010 - April 2022. As discussed earlier, lower magnitude intercept values correspond with less atmospheric noise and vice versa. Figure 4b indicates that JJA is a period of calm atmospheric noise while DJF is a period of disturbed atmospheric noise. Similar to DART 21420, DART 46407's seasonality appears to coincide with the extratropical

https://doi.org/10.5194/egusphere-2025-5764
Preprint. Discussion started: 7 January 2026

cyclone season in the north Pacific, which multiple sources attribute to producing IGW events (Webb et al., 1991; Aucan and Ardhuin, 2013; Rawat et al., 2014; Rabinovich and Eblé, 2015).

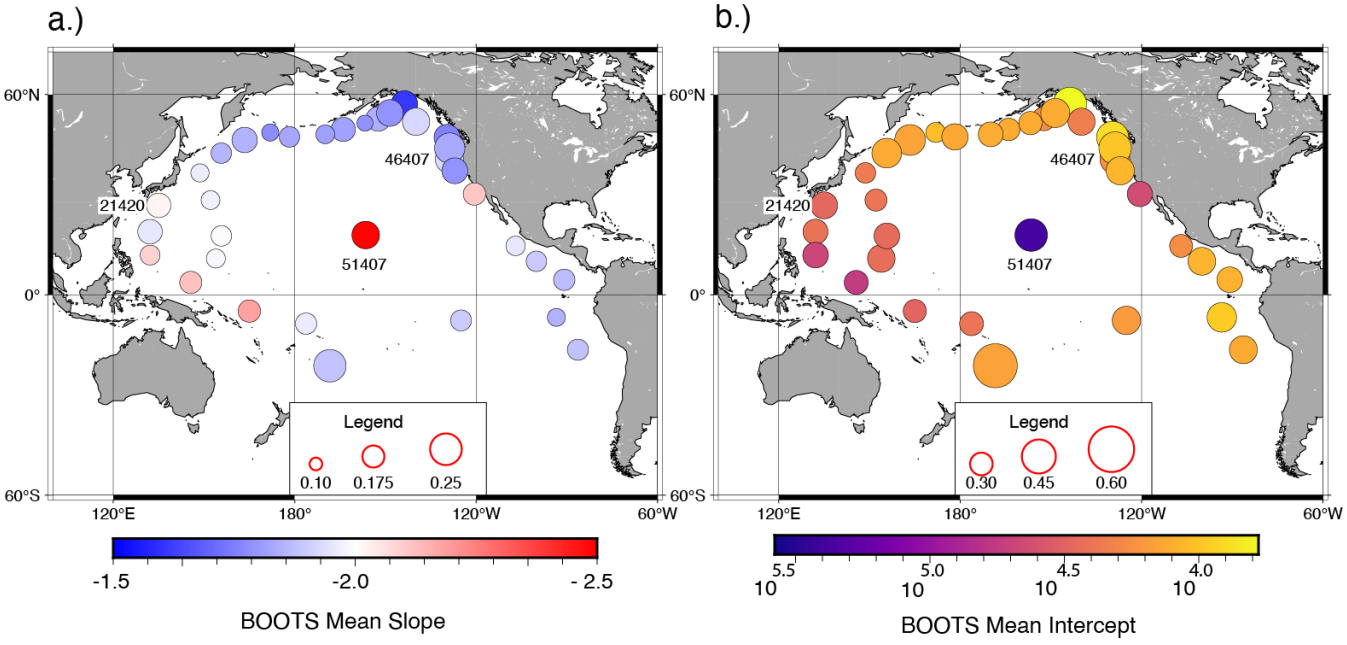

Figure 5. a.) Mean slope of the BOOTS across the Pacific basin for each station's entire temporal coverage. Color of the circle corresponds to the mean value of the BOOTS slope. Circle size corresponds to the standard deviation of the slop. b.) Intercept of the BOOTS across the Pacific basin. Color of the circle corresponds to the mean value of the intercept. Circle size corresponds to the standard deviation of the intercept.

We demonstrate in Figure 5 that the other DART stations fall somewhere between the previously demonstrated behaviors. We note that sites with behavior similar those similar to DART 21420 are its neighbors in the West Pacific. Similarly, DART 46407's neighbors in the northeast Pacific exhibit similar behaviors. The exception to this trend is DART 51407 — the DART nearest Hawaii (Figures 2 and 5) . This station is notable for the sheltering effect it experiences from the Hawaiian Big Island (Webb et al., 1991; Rawat et al., 2014). It is not affected like other DART stations by meteorological events in the North Pacific, naturally filtering out the noise in the BOOTS that is generated from the region. However, we find it is susceptible to meteorologically induced IGW events from the South and Southeast Pacific.

3.3 Infragravity waves in the BOOTS

Next, we show that the chief driver of the spatiotemporal variability of the BOOTS slope and intercept are most likely IGW.

https://doi.org/10.5194/egusphere-2025-5764
Preprint. Discussion started: 7 January 2026

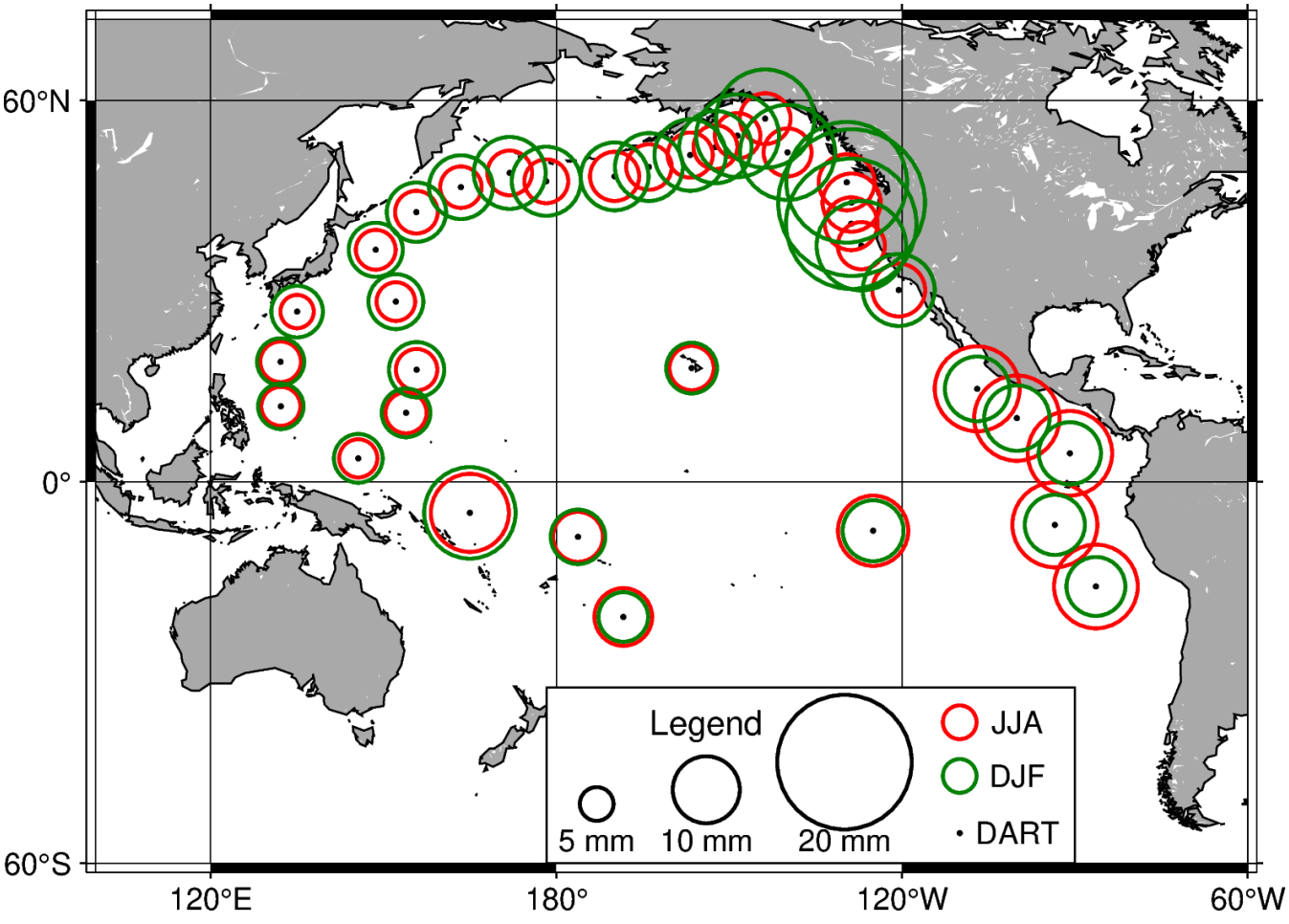

Figure 6. Infragravity wave heights for the time periods of JJA (red circles) and DJF (green circles). DART locations are shown as black dots.

3.3.1 Spatiotemporal Effects of IGWs

We find that the highest values of H_{IG} and the strongest seasonality are in the northeast Pacific within the Gulf of Alaska and in the area of the CSZ (Figure 6). $H_{IG,DJF}$ is a factor of 2-3 larger in these regions than $H_{IG,JJA}$. We observe that H_{IG} values decrease westward from the Gulf of Alaska and the CSZ. Aucan and Ardhuin (2013) attribute this effect to the convex shape of the Alaska peninsula and the Aleutian Islands, where IGW free energy can disperse over a wider ocean region. Our areas of high H_{IG} are in line with the values measured by Aucan and Ardhuin (2013) and Rawat et al. (2014).

We find that, in the equatorial latitudes of the Pacific, the values of H_{IG} are lower and have a less pronounced seasonality. From Mexico to Peru, H_{IG} has a reversed seasonality signal. This result is in line with the results of Filloux et al. (1991);

https://doi.org/10.5194/egusphere-2025-5764
Preprint. Discussion started: 7 January 2026

Aucan and Ardhuin (2013); Rawat et al. (2014). However, we find, in addition to austral winter storms in the south Pacific, that tropical systems in the East Pacific are another likely source of IGW events.

3.3.2 Meteorological impacts on the BOOTS noise

Numerous works in the literature describes that IGWs and the BOOTS are impacted by meteorological events yet refrain from showing these systems' meteorological set ups (Kulikov et al., 1983; Filloux et al., 1991; Rabinovich, 1997; Aucan and Ardhuin, 2013; Rawat et al., 2014). Here we use weather model output to connect days of high H_{IG} values to specific types of meteorological systems. We choose the High Resolution Rapid Refresh (HRRR), European Centre for Medium-Range Weather Forecasts (ECMWF) weather and wave models, and the Global Ensemble Forecast System (GEFS) to investigate storm systems across the Pacific, where we have shown in earlier sections that H_{IG} values are high. We utilize a variety of models due to the varying availability of model output for the time duration of our study. Model output is not always available for the time period of 2006-2022 due to storage or open data availability issues. Model output are processed using Herbie (Blaylock et al., 2017; Blaylock, 2024).

For the HRRR model, we visualize storms systems by using the maximum/composite radar reflectivity. For the ECMWF wave model, we visualize storm systems with the significant height of combined wind waves and swell forecast and geopotential height at 850 mb pressure level with 10 m winds plotted to visualize the wind field of the tropical and extratropical systems. For the GEFS, we use the mean member pressure reduced to mean sea level with 10 m winds plotted to visualize the wind field of the tropical and extratropical systems.

Figure 7a shows the ECMWF significant height of combined wind waves and swell for an extratropical storm that transits through the Gulf of Alaska during February. Storm systems that transit through this region are strong enough to elicit high H_{IG} values at the CSZ DART stations. They have combined wind waves and swell heights of 10-12 m in the Gulf of Alaska, yet only produce heights of 3-4 m over the CSZ. As Aucan and Ardhuin (2013) and Rawat et al. (2014) note, these storm systems produce conditions favorable for IGWs due to their storm track and intensity. For the February 10, 2022 storm, the system's center is located at $142°$W and $60°$N, yet it is producing widespread IGW impacts across the area, in spite of a high pressure system that has set up at $135°$W and $45°$N, Figure 7b and 7c. Low wind speeds in the high pressure area do not efficiently generate wind waves, so the wind generated waves and swell from the extratropical system can transit across the area with little to no impact.

In contrast, DARTs 43413 and 43412 show evidence for IGW events forced by tropical systems. Figure 8 shows the PPSD and PPSD signal for DART 43413 as Tropical Storm Kevin and Hurricane Linda pass to the northwest of the station. As seen with the CSZ DARTs, the stations along the Middle and South America Trenches experience higher H_{IG} values when transit close to the stations. Higher H_{IG} values for the DART stations off of South America are also experienced due to austral winter storms in JJA in the southern hemisphere.

https://doi.org/10.5194/egusphere-2025-5764
Preprint. Discussion started: 7 January 2026

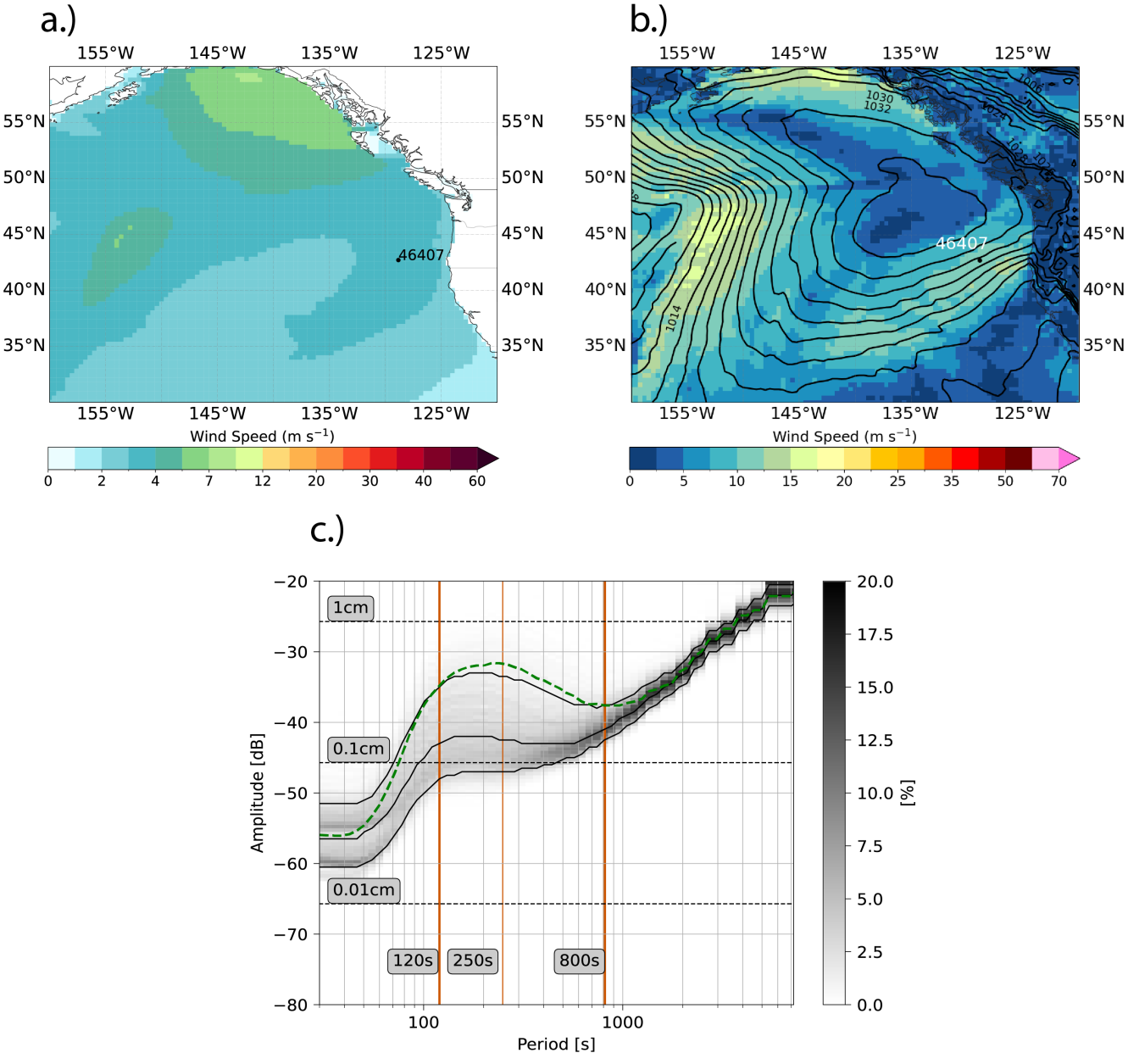

Figure 7. a.) ECMWF wave height model at 0.5° resolution for February 10, 2022 at 12 UTC. DART 46407 is shown by a black dot. b.) ECMWF model at 0.5° resolution for February 10, 2022 at 12 UTC. Geopotential height at 850 mbar is plotted at 50 m contours. 10 m wind is shown by filled contours. c.) PPSD for DART 46407 for the meteorological event signal during August 13, 2021. The signal is shown by the dashed green line.

https://doi.org/10.5194/egusphere-2025-5764
Preprint. Discussion started: 7 January 2026

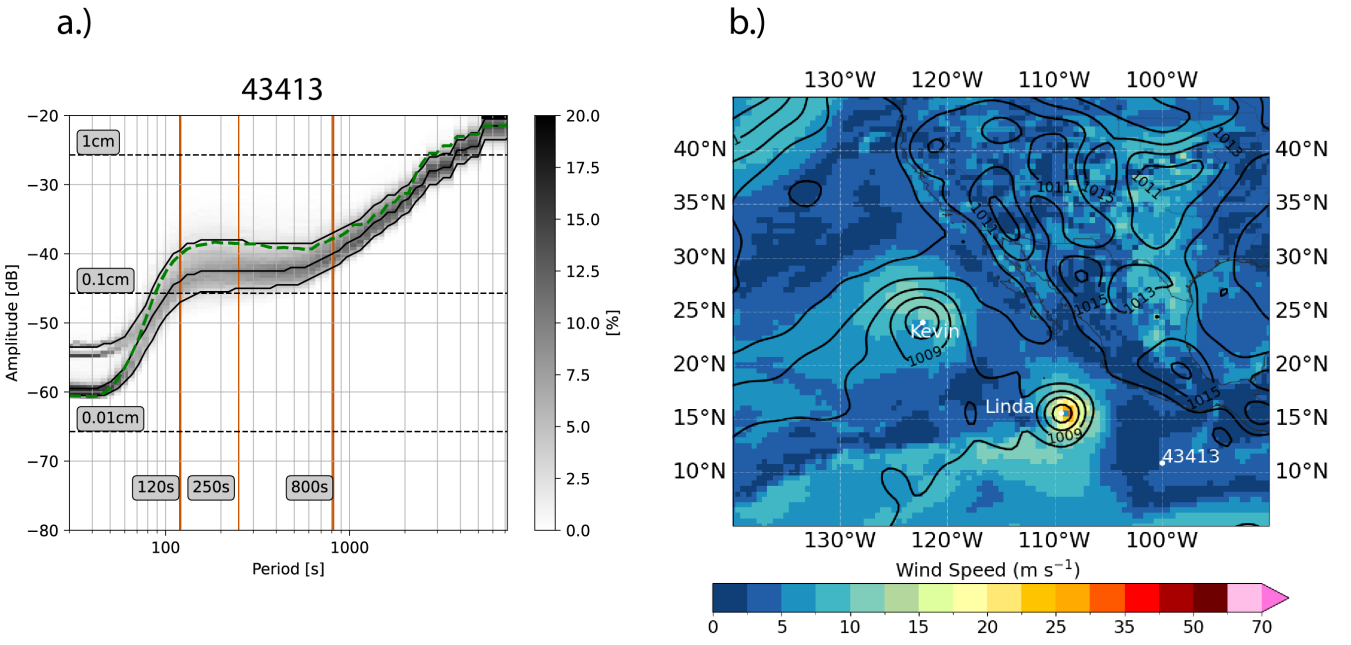

Figure 8. a.) PPSD for DART 43413. Meteorological event signal for August 13, 2021 is shown by the dashed green line. b.) GEFS model at 0.5° resolution for August 13, 2021 at 12 UTC. 10 m wind is shown to visualize the wind field of the tropical systems. Pressure reduced to mean sea level (MSL) pressure is shown by the black contours. Contours are plotted at 2 mbar intervals. DART 43413 is shown by a white dot. The approximate locations of tropical storm Kevin and Hurricane Linda's cores are shown by white dots.

3.4 Other temporal variations in BOOTS noise

So far, our discussion has been limited to the effects of IGWs on the noise profile of the BOOTS, but there are still other features in the PPSDs that we have yet to fully explain. Among these are the apparent bifurcation in noise profile for the short periods of 30 s - 80 s. These periods are outside the realm of the BOOTS, and they are subject to the instrument response. In fact, as shown in Figure 9, the high noise location is from 2011 and the low noise location is from 2021. It becomes clear from looking at the metadata that the DART sensor has been upgraded from the previous DART sensor to DART 4G. Indeed, for DARTs that have long records, this change in sensors is responsible for the bifurcation.

Still there are other temporal variations in the BOOTS noise of concern. One such is the manifestation of tsunami waves in the PPSD. We show in Figure 9 that tsunami waves do not have as much energy in the IGW periods as IGWs themselves. In fact, it is not until the end of the IGW band that tsunami amplitude energies are larger than those linked to IGWs. Indeed, it is not just for the 2021 Chignik tsunami that this feature is observed. It is also observed for the tsunamis from the 2020 Simeonof and 2020 Sand Point tsunamis, as shown in Figure 10. Again, in these events, the tsunami amplitude energy is smaller than those linked with IGW events in the IGW band, as they tend to 50^{th} percentile. And it indicates that tsunamis are not the main

https://doi.org/10.5194/egusphere-2025-5764
Preprint. Discussion started: 7 January 2026

driver of variation in these periods, for these events. A more robust reanalysis must be done to ascertain if this is true for more tsunami events.

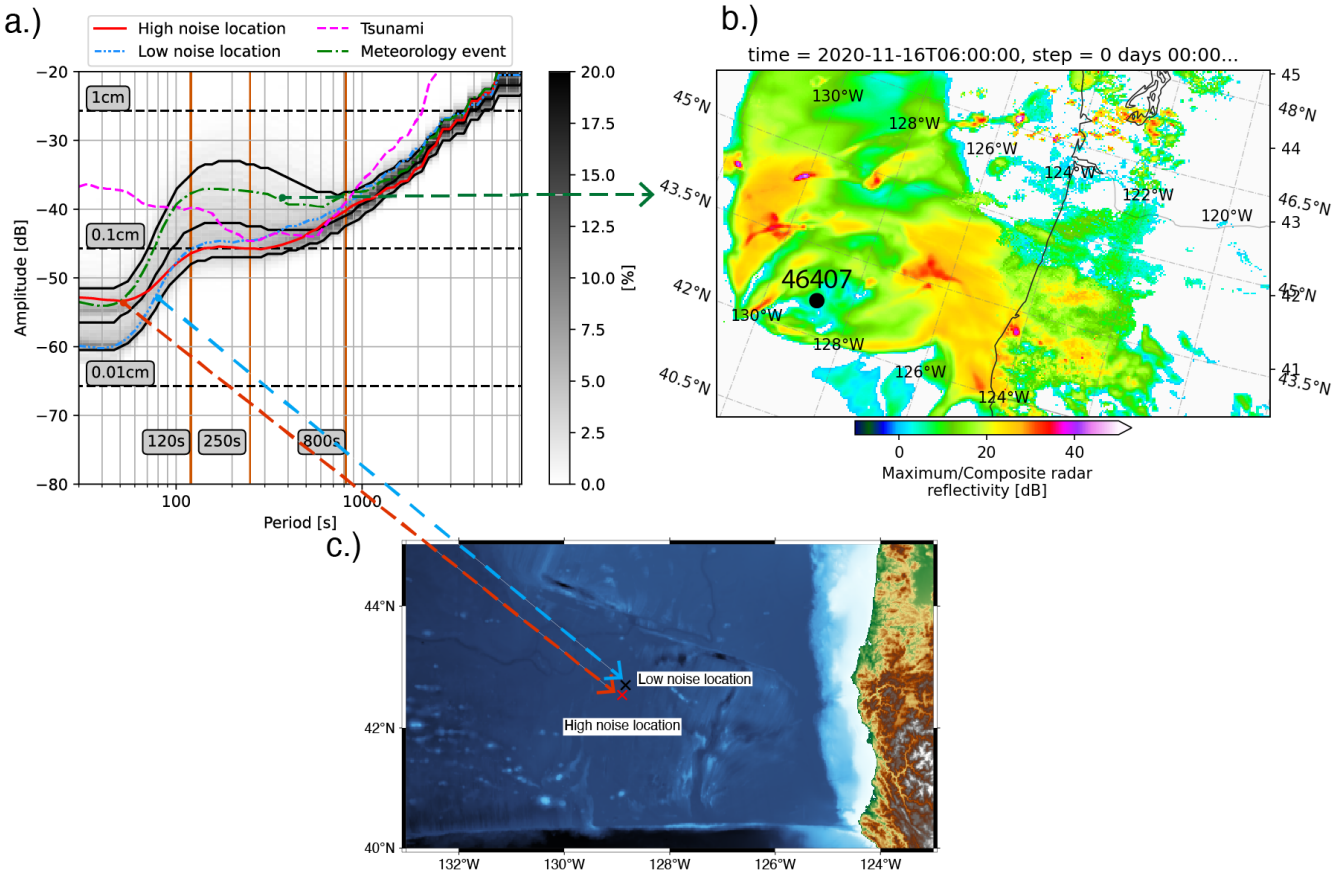

Figure 9. a.) PPSD for DART 46407. High noise location (red), low noise location (dash-dot-dot blue), meteorological event (dash-dot green), and tsunami (July 22, 2021 Chignik earthquake, dash magenta) PSDs are plotted for their respective occurrences. Arrows point to their respective phenomena in panels b.) and c.). b.) Meteorological event that occurred on November 16, 2020, at 0600 UTC which produced noise above the 10th percentile in the BOOTS. Maximum/Composite radar reflectivity from the 0600 UTC High Resolution Rapid Refresh (HRRR) model is shown. c.) Location of DART 46407 at a high noise location (UTC Day May 17, 2011, red x) and a low noise location (UTC day July 7, 2021, black x).

3.5 Spatial variations in the BOOTS noise PDFs

We have shown that the PPSDs BOOTS noise does not follow consistently the ω^{-2} reference power law, and that deviations from it follow seasonal patterns. We have also shown that these seasonal patterns arise from meteorological systems, which are efficient generators of IGWs in the North and East Pacific. We have also shown that the BOOTS noise is not determined by station location or by tsunami effects. We will next show how this affects the shape of the PDF of the noise profiles across

https://doi.org/10.5194/egusphere-2025-5764
Preprint. Discussion started: 7 January 2026

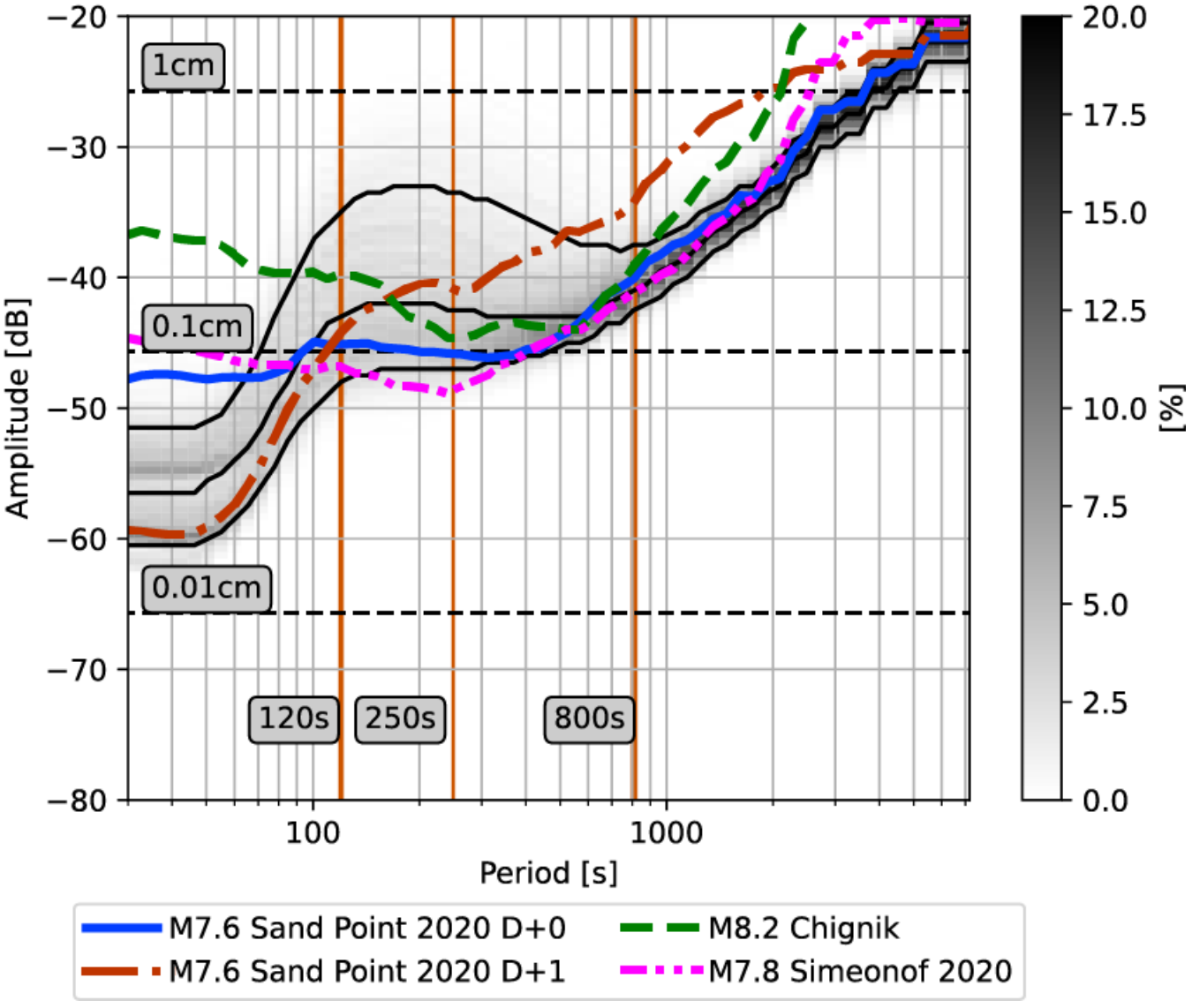

Figure 10. DART 46407 PPSD. The 2020 M7.8 Simeonof earthquake is shown by a dash-dot-dot magenta line (UTC Day July 22, 2020). The 2020 M7.6 Sand Point earthquake is shown in blue (UTC Day October 19, 2020) and by a dash-dot crimson line (UTC Day October 20, 2020). The 2021 Chignik earthquake is shown by a dashed green line (UTC Day July 21, 2021).

https://doi.org/10.5194/egusphere-2025-5764
Preprint. Discussion started: 7 January 2026

the Pacific basin. Figure 11a shows that there is no clear spatial clustering of PDFs for periods of 120 s. The Northeast Pacific,

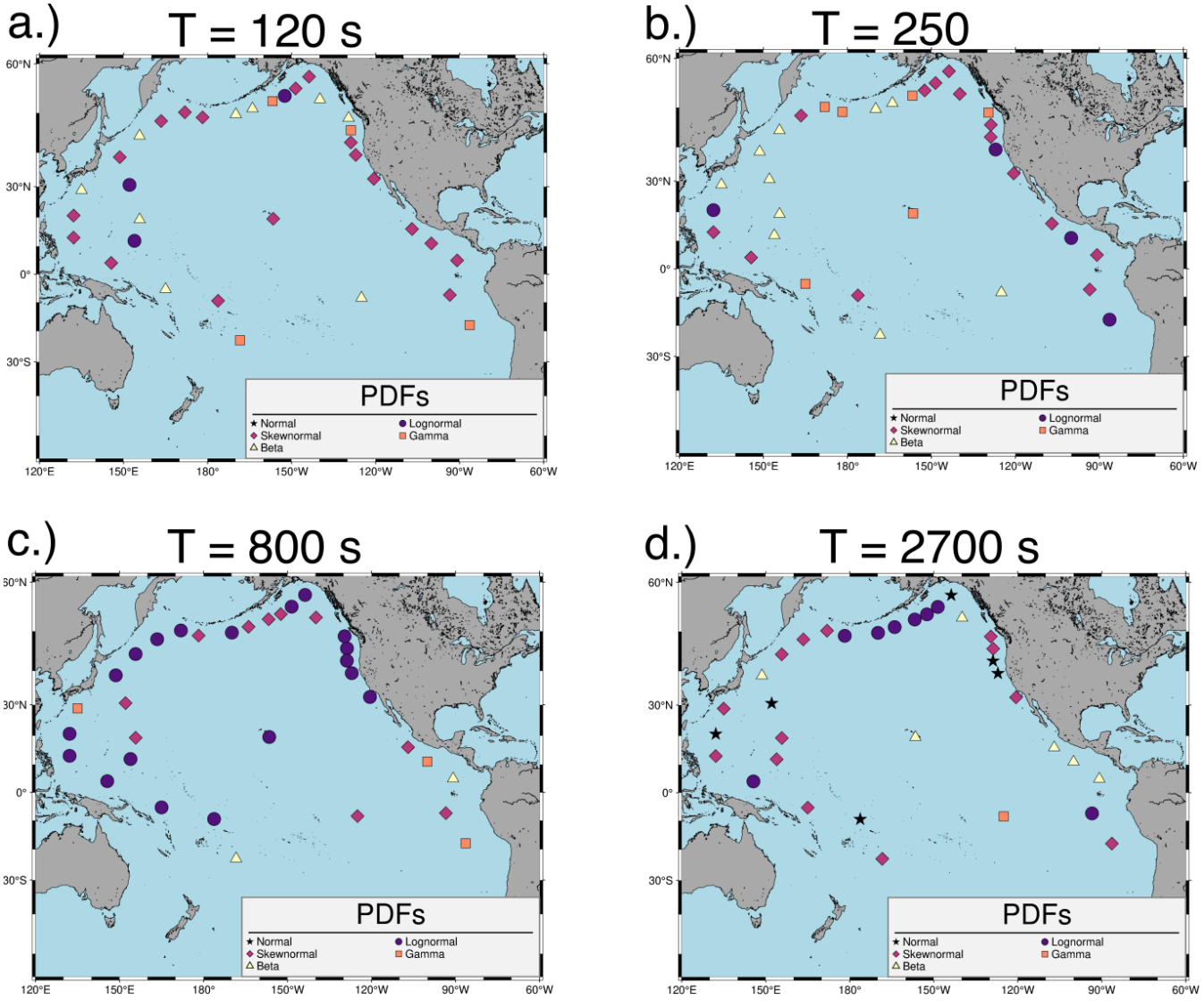

Figure 11. a.) Empirically best fitting probability distribution functions (PDFs) for the period of 120 s. Square represents the gamma distribution. Triangle represents the beta distribution. Circle represents the lognormal distribution. Star represents the normal distribution. Diamond represents the skewnormal distribution. The sequential magma colormap is used to differentiate the symbols. b.) Best fitting PDFs for the period of 250 s. c.) Best fitting PDFs for the period of 800 s. d.) Best fitting PDFs for the period of 2700 s.

which has the largest measurements of IGWs does not favor any one PDF. Instead, we see that any of four best describe the noise shape: beta, gamma, log normal, and skew normal. Not only is this true of the Northeast Pacific, but for the rest of the basin as well! What is discernible from the spatial distribution is that the beta and gamma distributions are not found anywhere

https://doi.org/10.5194/egusphere-2025-5764
Preprint. Discussion started: 7 January 2026

where H_{IG} values are < 10 mm. Figure 11b shows a stronger spatial correlation at a period of 250 s. Areas of high H_{IG} either follow skew normal or log normal PDFs, as seen in the Northeast Pacific. Although, some DARTs are best fit by the beta and gamma distributions. The exception to this are the DARTs in the Northwest Pacific, which are predominately described by the beta distribution. Figure 11c shows an even stronger spatial correlation of log and skew normal distributions in the North Pacific. All but three DART stations in the period of 800 s are described by the two, with the exceptions being DART 21420, and the two immediately north of the equator. In the southern hemisphere, the furthest south DARTs in Figure 11c are best described by the beta and gamma distributions. Figure 11d shows that nearly every DART station in the North Pacific is described by either the log normal, skew normal, or normal distribution. The only exceptions being the DART stations off of Central America, the DART station west of Queen Charlotte Island in the Northeast Pacific, the DART station east of Honshu, and DART 51407 near Hawaii. Along with the North Pacific exceptions, the DART station in South Central Pacific is best described by the gamma distribution — the sole DART for the period of 2700 s. It should be noted that the PDF variability does not appear to follow a clear pattern based on length of available data. DART 46414 (south of Chirikov Island, Alaska) and DART 46415 (west of Queen Charlotte Island, Canada) were deployed at the same time with the same type of sensor, yet have two different noise profiles through the four periods of interest. This fact means that the PDF fits are not correlated with the length of data and type of DART sensor, but are more correlated with the physical processes going on where the stations are located.

4 Discussion and Conclusion

The current study presents findings from empirically fitting PDFs on four periods of interest throughout the BOOTS for 1-15 years of 15 s DART station data. This study was designed to investigate the noise distribution of the BOOTS and its relationship to the reference power law of ω^{-2}. We find that the PDFs are mostly non-normal for the short periods of 120 s and 250 s, which are within the portion of the BOOTS that interacts with atmospherically generated IGW (Roger, 2024). In addition, we find that longer periods outside the IGW interaction band; likewise, have non-normal PDFs but to a much lesser extent than the IGW interaction band.

We cannot determine what causes the data to deviate from Gaussianity in the longer periods. This finding poises an open question that we cannot answer. For shorter periods, IGWs may potentially affect the non-Gaussianity of the data, but we cannot adequately determine if what affects the longer periods affects the shorter periods. We cannot adequately determine a physical mechanism that is not a correlation.

While current implementations of DA and ML make use of low computational cost algorithms, our findings suggest that they may struggle with adequately modeling tsunami impacts. These results suggest that more complex DA and ML algorithms must be adopted to deal with data that deviate from Gaussianity. This result is not new (Zhang et al., 2004; Anderson, 2010; Poterjoy and Anderson, 2016; Chan et al., 2020; Poterjoy, 2022). Geophysical data have been known to deviate from Gaussianity — particularly in weather forecasting applications (Anderson and Anderson, 1999). It has been noted, in DA literature, that non-normal PDFs can pose challenges for Gaussian-based DA algorithms, which can manifest as unphysical ensembles, leading to

https://doi.org/10.5194/egusphere-2025-5764
Preprint. Discussion started: 7 January 2026

egregious errors in forecast lead times (Poterjoy, 2022). However, this fact is object of future study, as it is unclear how this may manifest for tsunami impacts, especially as it pertains to inundation and flow velocity in shallow water.

The argument against our claims is that previous tsunami DA and ML applications have done well with Gaussian assumptions (Maeda et al., 2015; Gusman et al., 2016; Sheehan et al., 2019; Yang et al., 2019; Someya and Furumura, 2025). Chan et al. (2020) notes that this assumption while being imperfect is functional. Minamide and Zhang (2017) detail the consequences of a functional Gaussian assumption manifesting as large departures from first guesses and observations. In large part, the consequences in tsunami DA are minimized because importance is given to the accuracy of the first arrivals' wave heights — that is because they are considered to be linear (Melgar and Bock, 2013). This choice of accuracy metric masks the unwanted effects of nonlinear features (e.g., shoaling and dispersion) that tsunami models struggle with modeling. But model errors are an intrinsic part of the DA process (Zhang et al., 2004; Wikle and Berliner, 2007; Anderson, 2010; Poterjoy and Anderson, 2016; Minamide and Zhang, 2017; Chan et al., 2020; Poterjoy, 2022)! By making such assumptions, tsunami DA algorithms cannot be used for the more consequential tsunami impact forecasting, such as constraining the error on inundation and flow velocity from events.

Indeed, the main takeaway of this study is that DART data do not strictly adhere to Gaussianity assumptions within the BOOTS, and that this is correlated with IGW generating atmospheric events. We are unable to answer if these assumptions break down for tsunami events as well. These features may also manifest in other water level detection instruments like in ocean bottom distributed acoustic sensing cables.

5 Code and Data Availability

. DART BPR data is available at https://www.ngdc.noaa.gov/hazard/dart/. Records of tsunamis in the Pacific basin are available at https://data.noaa.gov/metaview/page?xml=NOAA/NESDIS/NGDC/MGG/Hazards/iso/xml/G02151.xml&view=getDataView. The Herbie python code is available from GitHub at https://github.com/blaylockbk/Herbie and archived on Zenodo at Blaylock (2024). The PPSDs were generated using the multitaper python package available from GitHub at https://github.com/gaprieto/multitaper and documented by Prieto (2022). Table S1 and other codes necessary for the study are available from GitHub at https://github.com/ssantellanes/BOOTS and archived on Zenodo at Santellanes (2024).

6 Author Contribution

. SS contributed to conceptualization, methodology, software, formal analysis, investigation, writing, reviewing, editing, and visualization. DM contributed to conceptualization, methodology, resources, reviewing, editing, supervision, and funding acquisition.

https://doi.org/10.5194/egusphere-2025-5764
Preprint. Discussion started: 7 January 2026

7 Competing Interests

. The authors declare that they have no conflict of interest.

8 Acknowledgements

. We would like to thank Aaron Sweeney for helpful discussions on processing DART data. A portion of this work used code generously provided by Brian Blaylock's Herbie python package (https://doi.org/10.5281/zenodo.4567540). We would also like to thank the Gordon and Betty Moore Foundation for funding the grant SMART Subsea Cables: Implementing for Geophysics, Early Warning and Oceans, Vanuatu-New Caledonia to Global subward MA2169.

https://doi.org/10.5194/egusphere-2025-5764
Preprint. Discussion started: 7 January 2026

References

Anderson, J. L.: A Non-Gaussian Ensemble Filter Update for Data Assimilation, Monthly Weather Review, 138, 4186 – 4198, https://doi.org/10.1175/2010MWR3253.1, 2010.

Anderson, J. L. and Anderson, S. L.: A Monte Carlo Implementation of the Nonlinear Filtering Problem to Produce Ensemble Assimilations and Forecasts, Monthly Weather Review, 127, 2741 – 2758, https://doi.org/10.1175/1520-0493(1999)127<2741:AMCIOT>2.0.CO;2, 1999.

Aucan, J. and Ardhuin, F.: Infragravity waves in the deep ocean: An upward revision: INFRAGRAVITY WAVES IN THE DEEP OCEAN, Geophysical Research Letters, 40, 3435–3439, https://doi.org/10.1002/grl.50321, 2013.

Blaylock, B. K.: Herbie: Retrieve Numerical Weather Prediction Model Data, https://doi.org/10.5281/zenodo.10759470, 2024.

Blaylock, B. K., Horel, J. D., and Liston, S. T.: Cloud archiving and data mining of High-Resolution Rapid Refresh forecast model output, Computers & Geosciences, 109, 43–50, https://doi.org/https://doi.org/10.1016/j.cageo.2017.08.005, 2017.

Chan, M.-Y., Anderson, J. L., and Chen, X.: An efficient bi-Gaussian ensemble Kalman filter for satellite infrared radiance data assimilation, Monthly Weather Review, 148, 5087–5104, 2020.

Filloux, J. H., Luther, D., and Chave, A.: Long-term seafloor measurement of water pressure: Normal modes and infragravity waves, Proceedings of the XXth General Assembly IUGG, 1991.

Gica, E.: Development of the forecast propagation database for NOAA's Short-term Inundation Forecast for Tsunamis (SIFT), 2008.

Gusman, A. R., Sheehan, A. F., Satake, K., Heidarzadeh, M., Mulia, I. E., and Maeda, T.: Tsunami data assimilation of Cascadia seafloor pressure gauge records from the 2012 Haida Gwaii earthquake, Geophysical Research Letters, 43, 4189–4196, https://doi.org/https://doi.org/10.1002/2016GL068368, 2016.

Kohler, M. D., Bowden, D. C., Ampuero, J.-P., and Shi, J.: Globally scattered 2011 Tohoku tsunami waves from a seafloor sensor array in the northeast Pacific Ocean, Journal of Geophysical Research: Solid Earth, 125, e2020JB020 221, 2020.

Kulikov, E. A., Rabinovich, A. B., Spirin, A. I., Poole, S. L., and Soloviev, S. L.: Measurement of tsunamis in the open ocean, Marine Geodesy, 6, 311–329, https://doi.org/10.1080/15210608309379465, 1983.

Liu, C. M., Rim, D., Baraldi, R., and LeVeque, R. J.: Comparison of machine learning approaches for tsunami forecasting from sparse observations, Pure and Applied Geophysics, 178, 5129–5153, 2021.

Maeda, T., Obara, K., Shinohara, M., Kanazawa, T., and Uehira, K.: Successive estimation of a tsunami wavefield without earthquake source data: A data assimilation approach toward real-time tsunami forecasting, Geophysical Research Letters, 42, 7923–7932, 2015.

McNamara, D. E. and Buland, R.: Ambient Noise Levels in the Continental United States, Bulletin of the Seismological Society of America, 94, 1517–1527, https://doi.org/10.1785/012003001, 2004.

Melgar, D. and Bock, Y.: Near-field tsunami models with rapid earthquake source inversions from land- and ocean-based observations: The potential for forecast and warning: TSUNAMI MODELS WITH RAPID INVERSIONS, Journal of Geophysical Research: Solid Earth, 118, 5939–5955, https://doi.org/10.1002/2013JB010506, 2013.

Melgar, D. and Ruiz-Angulo, A.: Long-lived tsunami edge waves and shelf resonance from the M8. 2 Tehuantepec earthquake, Geophysical Research Letters, 45, 12–414, 2018.

Minamide, M. and Zhang, F.: Adaptive Observation Error Inflation for Assimilating All-Sky Satellite Radiance, Monthly Weather Review, 145, 1063 – 1081, https://doi.org/10.1175/MWR-D-16-0257.1, 2017.

https://doi.org/10.5194/egusphere-2025-5764
Preprint. Discussion started: 7 January 2026

Mulia, I. E., Ueda, N., Miyoshi, T., Gusman, A. R., and Satake, K.: Machine learning-based tsunami inundation prediction derived from offshore observations, Nature Communications, 13, 5489, 2022.

NCEI: National Geophysical Data Center / World Data Service: NCEI/WDS Global Historical Tsunami Database, https://doi.org/10.7289/V5PN93H7, accessed: 2024/03/14.

NCEI: Deep-Ocean Assessment and Reporting of Tsunamis (DART(R)), https://doi.org/10.7289/V5F18WNS, accessed: 2024/02/24, 2005.

Poterjoy, J.: Implications of multivariate non-Gaussian data assimilation for multiscale weather prediction, Monthly Weather Review, 150, 1475–1493, 2022.

Poterjoy, J. and Anderson, J. L.: Efficient Assimilation of Simulated Observations in a High-Dimensional Geophysical System Using a Localized Particle Filter, Monthly Weather Review, 144, 2007 – 2020, https://doi.org/10.1175/MWR-D-15-0322.1, 2016.

Prieto, G. A.: The *Multitaper* Spectrum Analysis Package in Python, Seismological Research Letters, 93, 1922–1929, https://doi.org/10.1785/0220210332, 2022.

Rabinovich, A. B.: Spectral analysis of tsunami waves: Separation of source and topography effects, Journal of Geophysical Research: Oceans, 102, 12 663–12 676, https://doi.org/10.1029/97JC00479, 1997.

Rabinovich, A. B.: Twenty-seven years of progress in the science of meteorological tsunamis following the 1992 Daytona Beach event, Pure and Applied Geophysics, 177, 1193–1230, 2020.

Rabinovich, A. B. and Eblé, M. C.: Deep-Ocean Measurements of Tsunami Waves, Pure and Applied Geophysics, 172, 3281–3312, https://doi.org/10.1007/s00024-015-1058-1, 2015.

Rabinovich, A. B., Candella, R. N., and Thomson, R. E.: The open ocean energy decay of three recent trans-Pacific tsunamis: TSUNAMI ENERGY DECAY, Geophysical Research Letters, 40, 3157–3162, https://doi.org/10.1002/grl.50625, 2013.

Raissi, M., Perdikaris, P., and Karniadakis, G. E.: Physics Informed Deep Learning (Part I): Data-driven Solutions of Nonlinear Partial Differential Equations, https://arxiv.org/abs/1711.10561, 2017.

Rawat, A., Ardhuin, F., Ballu, V., Crawford, W., Corela, C., and Aucan, J.: Infragravity waves across the oceans: Following Infra-Gravity Wave Bursts, Geophysical Research Letters, 41, 7957–7963, https://doi.org/10.1002/2014GL061604, 2014.

Roger, J.: Records of the 5 March 2021 Raoul Island transoceanic tsunami around the Pacific Ocean, New Zealand Journal of Geology and Geophysics, 67, 467–482, https://doi.org/10.1080/00288306.2023.2225859, 2024.

Santellanes, S. R.: ssantellanes/BOOTS: v1.0.0, https://doi.org/https://doi.org/10.5281/zenodo.10835239, 2024.

Sheehan, A. F., Gusman, A. R., and Satake, K.: Improving Forecast Accuracy With Tsunami Data Assimilation: The 2009 Dusky Sound, New Zealand, Tsunami, Journal of Geophysical Research: Solid Earth, 124, 566–577, https://doi.org/https://doi.org/10.1029/2018JB016575, 2019.

Someya, M. and Furumura, T.: Physics-informed neural networks for offshore tsunami data assimilation, Geophysical Journal International, 242, ggaf243, https://doi.org/10.1093/gji/ggaf243, 2025.

Titov, V. V., Gonzalez, F. I., Bernard, E. N., Eble, M. C., Mofjeld, H. O., Newman, J. C., and Venturato, A. J.: Real-Time Tsunami Forecasting: Challenges and Solutions, Natural Hazards, 35, 35–41, https://doi.org/10.1007/s11069-004-2403-3, 2005.

Webb, S. C., Zhang, X., and Crawford, W.: Infragravity waves in the deep ocean, Journal of Geophysical Research: Oceans, 96, 2723–2736, https://doi.org/10.1029/90JC02212, 1991.

Wikle, C. K. and Berliner, L. M.: A Bayesian tutorial for data assimilation, Physica D: Nonlinear Phenomena, 230, 1–16, 2007.

Yang, Y., Dunham, E. M., Barnier, G., and Almquist, M.: Tsunami Wavefield Reconstruction and Forecasting Using the Ensemble Kalman Filter, Geophysical Research Letters, 46, 853–860, https://doi.org/https://doi.org/10.1029/2018GL080644, 2019.

https://doi.org/10.5194/egusphere-2025-5764
Preprint. Discussion started: 7 January 2026

Zhang, F., Snyder, C., and Sun, J.: Impacts of Initial Estimate and Observation Availability on Convective-Scale Data Assimilation with an Ensemble Kalman Filter, Monthly Weather Review, 132, 1238 – 1253, https://doi.org/10.1175/1520-0493(2004)132<1238:IOIEAO>2.0.CO;2, 2004.